Chemical Science

ROYAL SOCIETY OF CHEMISTRY

EDGE ARTICLE

View Article Online
View Journal | View Issue

Cite this: *Chem. Sci.*, 2025, **16**, 11530

All publication charges for this article have been paid for by the Royal Society of Chemistry

Polymorphism and phase transformation tuned luminescence and mechanistic insights in nonconventional luminophores†

Anze Li, Zihao Zhao, Guangxin Yang, Qiang Zhang, Xiang Chen and Wang Zhang Yuan *

Nonconventional luminophores (NCLs) are attracting significant attention for their unique properties and applications. However, the lack of a comprehensive mechanistic understanding impedes their further development. Particularly, a recurring assumption that impurities are responsible for the luminescence has hindered progress. To elucidate the emission mechanism, we report tunable intrinsic emission from highly purified gemini aliphatic quaternary ammonium salts (GAQASs), leveraging their polymorphism. We demonstrate that polymorphism-dependent luminescence arises from distinct molecular packings and consequent varied clustering states. Specifically, denser ion clustering enhances charge transfer and recombination, heavy atom effects and conformational rigidity, thereby accelerating radiative triplet decay and intersystem crossing, while suppressing nonradiative triplet decay, ultimately leading to enhanced phosphorescence. Furthermore, GAQAS crystals undergo irreversible phase transformations upon heating, which partially disrupt intermolecular interactions, thus allowing for tunable emission. This polymorphism and phase transformation regulated luminescence in GAQASs strongly suggests that intrinsic factors, rather than impurities, are responsible for the observed emission, and are consistent with the clustering-triggered emission mechanism. Our findings establish a direct link between molecular packing, electronic structure and luminescent properties in NCLs. This study advances the mechanistic understanding of NCL luminescence, demonstrating an effective strategy for tunable emission *via* polymorphism and phase transformation.

Received 24th March 2025
Accepted 19th May 2025

DOI: 10.1039/d5sc02250a

rsc.li/chemical-science

Introduction

Nonconventional luminophores (NCLs), lacking extensive conjugation, have garnered significant interest due to their unique structure, facile preparation, rich resources, good biocompatibility, intriguing photoluminescence (PL) and versatile applications.[1–9] These combined advantages render them fundamentally important and technically attractive. Oxidation,[10] carbonyl (C=O) aggregation,[11] impurities,[12,13] short hydrogen bonding[14,15] and others, have been proposed to explain the PL emission from diverse systems, but these explanations often fall short of fully accounting for the observed phenomena and may even contradict observations in other NCL systems. In contrast, the clustering-triggered emission (CTE) mechanism posits that clustering of electron-rich moieties promotes electron delocalization and concomitant conformational rigidity of the clusters, consequently, leading to bright emission.[16–19] The CTE mechanism not only applies to a wide range of nonconventional luminophores and has been validated in diverse systems, but also offers a unifying framework for understanding their emissive behaviour.[20–25] However, persisting debates about the fundamental emission mechanism and a limited understanding of exciton dynamics continue to impede the rational design of new and improved NCLs, particularly with regard to the confounding influence of impurity-related emission,[12,13] which further complicates the elucidation of underlying mechanisms and photophysical properties. Therefore, to overcome these challenges and pave the way for the development of advanced NCLs, a rigorous and comprehensive investigation of their fundamental mechanisms and photophysical properties is essential.

Polymorphism offers an effective strategy for generating diverse crystals with well-defined structures and molecular packings.[26,27] This approach offers advantages for regulating PL and gaining insights into underlying mechanisms, while circumventing tedious synthesis.[28–30] However, achieving truly

State Key Laboratory of Synergistic Chem-Bio Synthesis, School of Chemistry and Chemical Engineering, Frontiers Science Center for Transformative Molecules, Shanghai Key Lab of Electrical Insulation and Thermal Aging, Shanghai Jiao Tong University, No. 800 Dongchuan Rd., Minhang District, Shanghai 200240, China. E-mail: wzhyuan@sjtu.edu.cn

† Electronic supplementary information (ESI) available: Detailed experimental procedures, characterization data and photophysical data. CCDC 2325933 (10-Br-a), 2423179 (10-Br-b), 2423180 (8-Br-a), 2423182 (8-Br-b), 2423185 (10-I-H_2O), 2423191 (10-I-MeOH), and 2423192 (10-I-MeCN). For ESI and crystallographic data in CIF or other electronic format see DOI: https://doi.org/10.1039/d5sc02250a

distinct molecular packings in polymorphic nonconventional luminophores remains a challenge, with rare exceptions involving pseudopolymorphism arising from variations in microenvironments due to residual solvents.[31] Herein, we employed gemini aliphatic quaternary ammonium salts (GAQASs) as a model system because their unique gemini structure,[32,33] featuring inter-anchoring ionic bonds and flexible alkyl chains, facilitates the formation of polymorphs. By varying the crystallization solvents, we obtained diverse GAQAS polymorphs exhibiting different molecular packings and tunable PL (Fig. 1a and b). Notably, polymorphs 10-Br-b and 8-Br-b, characterized by enhanced ion clustering and conformational rigidity, compared with other polymorphs, exhibited improved phosphorescence (Fig. 1c), allowing us to correlate structure with activity. Furthermore, studies of 10-I polymorphs revealed that different solvents can induce distinct clustering states, thereby modulating their photophysical properties (Fig. 1d).

Further ultrafast spectroscopy and theoretical calculations indicated that shorter ionic distances and stronger ionic interactions enhance charge transfer/recombination and the heavy atom effect, thereby facilitating intersystem crossing (ISC) and triplet radiative decay. Notably, GAQAS crystals also exhibited heating-induced phase transformations, providing further mechanistic insights and a novel strategy for PL regulation. These findings not only definitively exclude oxidation/impurity-induced emission (phosphorescence) in our vigorously purified systems with well-defined structures, but also establish viable routes for PL regulation through polymorphism and phase transformation.

Results and discussion

Three GAQASs were synthesized in moderate yields (~60%) *via* the quaternarization of trimethylamine with dibromoalkanes or diiodoalkanes at room temperature, followed by thorough

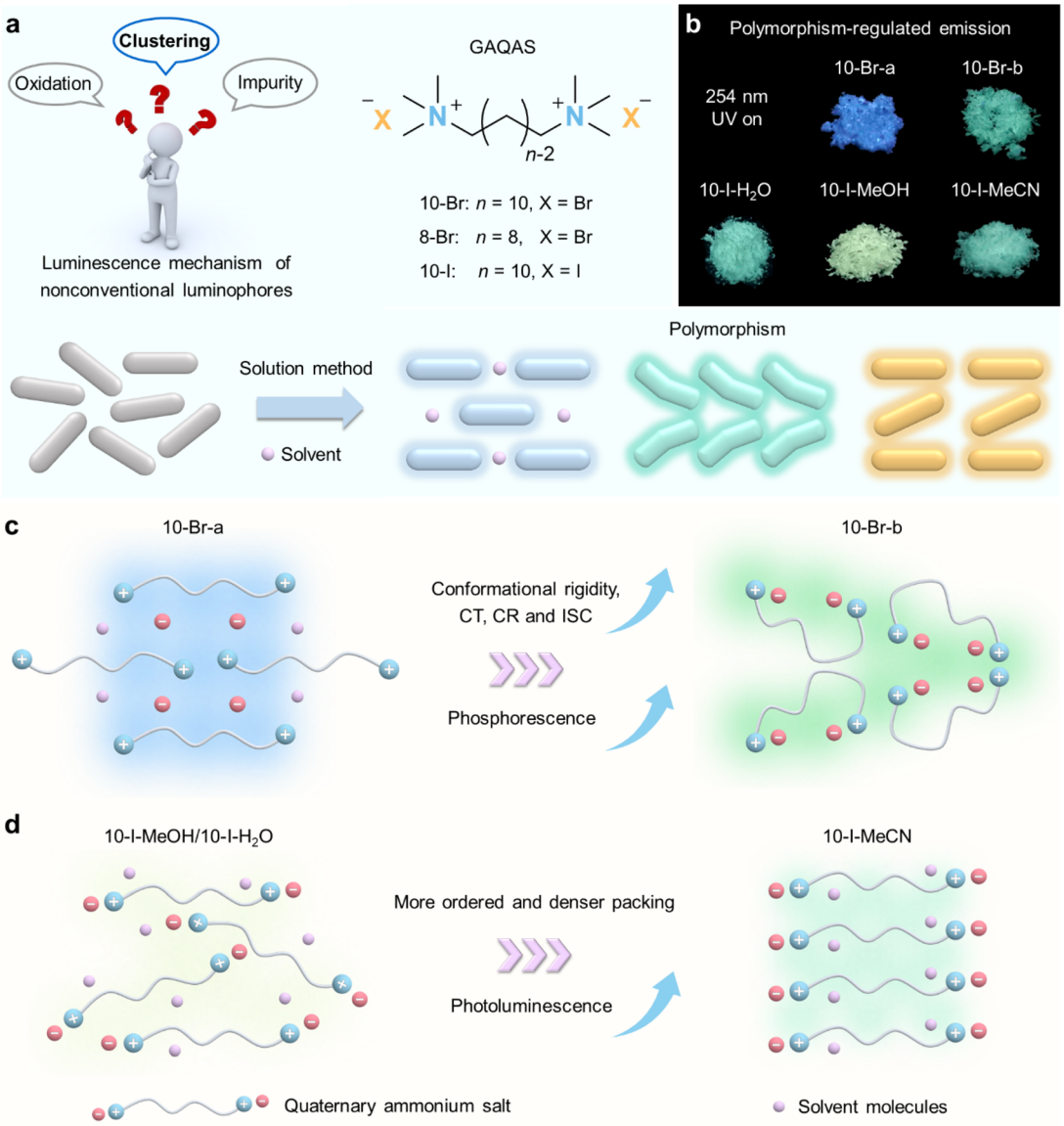

Fig. 1 (a) The design idea and chemical structures of GAQASs. (b) Luminescent photographs of different polymorphs of 10-Br and 10-I. Schematic illustration of polymorphism-regulated luminescence of (c) 10-Br and (d) 10-I.

purification processes. Their purities were confirmed by $^{1}H/^{13}C$ NMR, high-performance liquid chromatography (HPLC) and single-crystal X-ray diffraction (SCXRD) (Fig. S1–S4 and Tables S1–S3†).

To obtain GAQAS polymorphs, we cultivated single crystals using solvent evaporation, slow solution cooling and vapor diffusion with various solvents (Fig. 1a). We obtained different polymorphs distinguished by variations in molecular conformation, packing modes and solvent involvement. For example, the 10-Br-a polymorph, crystallized from an ethanol–water solution by slow evaporation,[33] belongs to the monoclinic space group $P2_1/c$, while the 10-Br-b polymorph, obtained by slow cooling of a saturated acetonitrile solution, belongs to the orthorhombic space group *Pbca* (Table 1). The relatively linear molecular conformation of 10-Br-a, in contrast to the bent conformation of 10-Br-b, leads to distinct molecular packing (Fig. 2a). Specifically, in 10-Br-a, each quaternary ammonium cation (N^+) interacts with two bromide anions (Br^-) and two water molecules (C–H···Br: 2.976 Å, C–H···O: 2.568 Å). The water molecules form strong noncovalent interactions with Br^- (O–H···Br: 2.554, 2.737 Å, Fig. S5a†), impeding the close approach of 10-Br cations and anions in its linear conformation. In contrast, the bent alkyl chain in 10-Br-b, along with the exclusion of water, leads to closer proximity between Br^- and N^+, resulting in stronger C–H···Br contacts (2.825–2.975 Å), shorter ionic distances (4.094–4.510 Å), denser molecular packing (1.413 $g\cdot cm^{-3}$) and more rigid conformations (Fig. S5b and Table S1†). Thus, molecular conformation and solvent involvement influence molecular packing in polymorphs, affecting their through-space electronic interactions and conformational rigidity.

With a shorter alkyl chain, we also obtained two polymorphs of 8-Br cultured by slow evaporation of aqueous ethanol solution (8-Br-a) and vapor diffusion in methanol-diethyl ether (8-Br-b), which exhibit nearly identical extended molecular conformations in the monoclinic space group $P2_1/n$ (Table S2†). Notably, in 8-Br-a, water participates in packing, forming strong hydrogen bonds with N^+ and Br^- (C–H···O: 2.412, 2.547 Å, O–H···Br: 2.510, 2.555 Å, Fig. 2b and S6†), significantly hindering their clustering. In comparison, 8-Br-b adopts an interlaced packing with richer and stronger C–H···Br interactions, facilitating the formation of ionic emissive clusters with rigid conformation. Thus, subtle conformational differences, coupled with solvent effects, dictate the resulting different molecular packing.

Using the iodide anion (I^-), 10-I yields three polymorphs, 10-I-H_2O, 10-I-MeOH and 10-I-MeCN, incorporating acetonitrile, methanol and water as solvates (Fig. 2c and Table S3†), respectively. On account of larger ionic radius and lower charge density of I^- anions, their coulombic interactions with N^+ are weakened. This, in turn, enhances interactions with solvent molecules, facilitating pseudopolymorphism.[34,35] Under methanol and water environments, 10-I-MeOH and 10-I-H_2O polymorphs crystallize in the monoclinic space group $C2/c$, showing relatively loose packing (1.324 and 1.315 g cm^{-3}, Table 1). In contrast, the 10-I-MeCN polymorph, crystallized in the triclinic space group $P\bar{1}$, exhibits an ordered and cooperative arrangement of 10-I and acetonitrile molecules, with the highest packing density (1.434 g cm^{-3}, Fig. 2c and S7†).

The prevalent polymorphism in GAQAS enables the regulation of PL, allowing us to establish strong structure-property relationships. Consequently, photophysical properties of these polymorphs were further examined. With an excitation wavelength (λ_{ex}) of 254 nm, 10-Br-a shows blue PL with a dominant peak at 395 nm, while 10-Br-b displays distinct green PL characterized by comparable dual emission bands at 375 and 510 nm (Fig. 3a and b). This change in PL colour is reflected in a shift of the CIE coordinates from (0.19, 0.16) to (0.25, 0.38) (Fig. 3c). As the λ_{ex} increases, the difference in PL colours between the two 10-Br polymorphs gradually diminishes (Fig. S8†). Under 365 nm UV irradiation, emission bands centered at 430 and 460 nm are observed in 10-Br-a and 10-Br-b (Fig. S9a and S10a†), respectively, resulting in similar blue-white PL. Meanwhile, the excitation spectra of 10-Br-a, measured at emission wavelengths (λ_{em}) of 403, 430 and 510 nm, exhibit similar trends, with an optimal λ_{ex} centered around 325 nm (Fig. S11a†). In contrast, the excitation spectra of 10-Br-b, measured at λ_{em} of 375, 460 and 510 nm, differ significantly, exhibiting maxima at 243, 365 and 257 nm, respectively (Fig. S11b†). This observation reveals the heterogeneous nature of emissive clusters in the two polymorphs and their varying response to λ_{ex},[32] further excluding the impurity mechanism, which would otherwise illustrate similar excitation spectra.

Table 1 Dynamic photophysical parameters of GAQAS polymorphs under 254 nm UV irradiation[a]

Crystal	Space group	Density [g cm^{-3}]	λ_f [nm]	λ_p [nm]	Φ_c [%]	Φ_f [%]	Φ_p [%]	τ_f [ns]	τ_p [ms]	k_{isc} [s^{-1}]	k_r^p [s^{-1}]	k_{nr}^p [s^{-1}]
10-Br-a	$P2_1/c$	1.299	395	515	3.1	2.0	1.1	5.7	409	6.2×10^7	0.08	2.4
10-Br-b	*Pbca*	1.413	375	515	11.5	2.7	8.8	4.8	882	1.6×10^8	0.13	1.0
8-Br-a	$P2_1/n$	1.392	402	530	8.3	5.4	2.9	6.1	137	5.7×10^7	0.60	6.7
8-Br-b	$P2_1/n$	1.372	430	515	22.4	11.2	11.2	7.8	292	6.4×10^7	0.77	2.6
10-I-H_2O	$C2/c$	1.315	355	535	0.8	0.01	0.79	2.6	60	3.8×10^8	0.13	16.5
10-I-MeOH	$C2/c$	1.324	370	535	1.7	0.3	1.4	2.6	124	3.2×10^8	0.14	7.9
10-I-MeCN	$P\bar{1}$	1.434	365	530	4.2	1.2	3.0	2.7	216	2.6×10^8	0.19	4.4

[a] $\Phi_c = \Phi_f + \Phi_p$; $\Phi_{isc} = \Phi_p/(\Phi_p + \Phi_f)$; $k_{isc} = \Phi_p/(\Phi_p + \Phi_f)\tau_f$; $k_r^p = (\Phi_p + \Phi_f)/\tau_p$; $k_{nr}^p = (1 - \Phi_p - \Phi_f)/\tau_p$. λ_f and λ_p are the PL maxima of fluorescence and phosphorescence of the polymorphs. Φ_c, Φ_f and Φ_p are the quantum efficiencies of total emission, fluorescence and phosphorescence of the polymorphs, respectively.

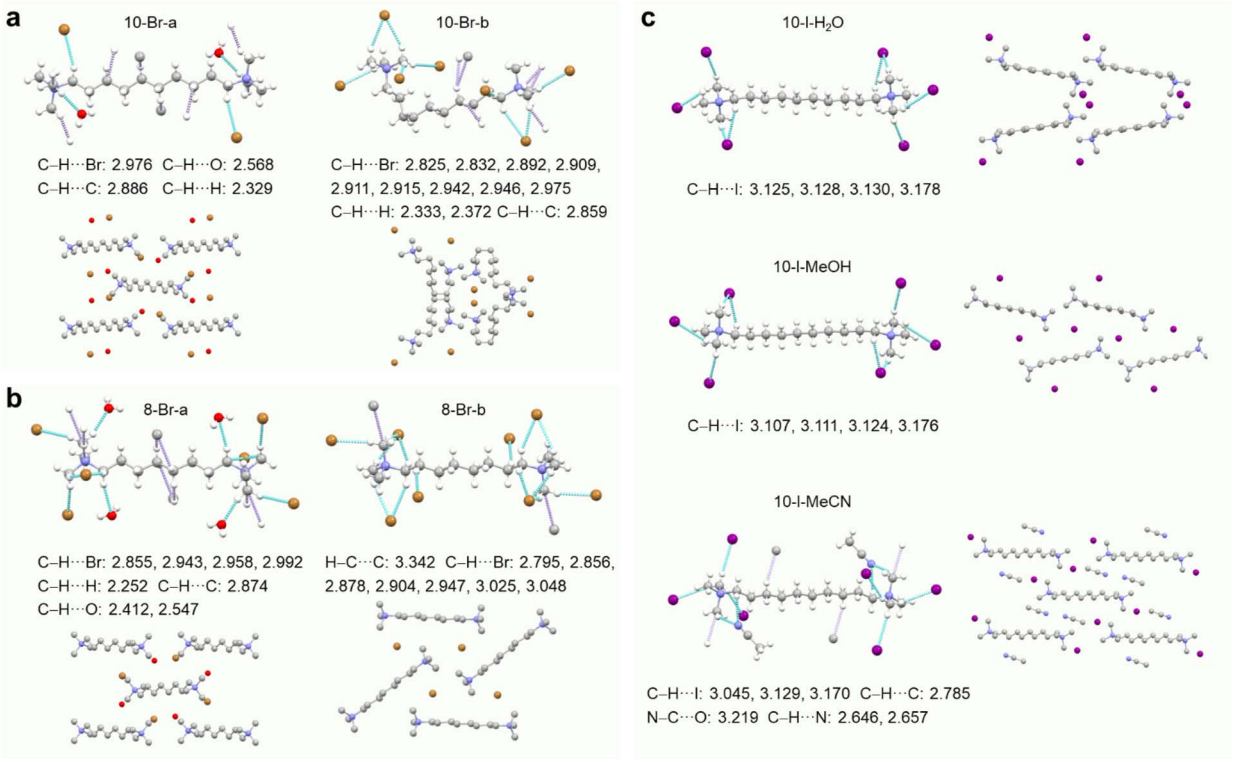

Fig. 2 Single-crystal structures with fragmental molecular packing of (a) 10-Br, (b) 8-Br and (c) 10-I polymorphs.

Despite significant differences in PL colours, both 10-Br polymorphs exhibit similar green afterglows after ceasing the 254 nm UV irradiation (Fig. 3a). Notably, the delayed ($t_d = 1$ ms) PL peaks of 10-Br-b coincide with the bands over 500 nm in prompt emission, with lifetime of hundreds of milliseconds (Fig. 3b–e and S10a–d†), indicating its persistent room

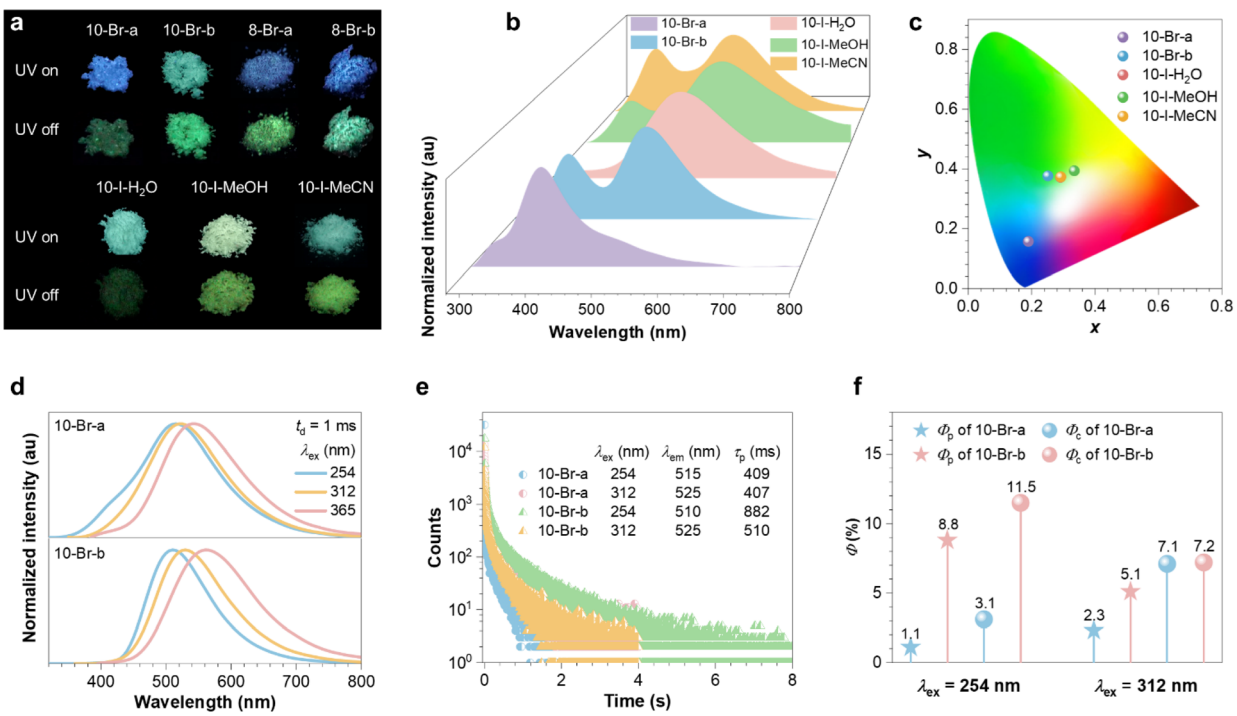

Fig. 3 (a) Luminescent photographs of three GAQAS polymorphs under and after ceasing the 254 nm UV irradiation. (b) Prompt emission spectra and (c) corresponding CIE coordinate diagram of 10-Br and 10-I polymorphs ($\lambda_{ex} = 254$ nm, the red and yellow dots overlap). (d) Delayed ($t_d = 1$ ms) emission spectra of 10-Br-a and 10-Br-b under different λ_{ex}s. (e) τ_p and (f) Φ_c/Φ_p of 10-Br polymorphs under 254 and 312 nm UV irradiations.

temperature phosphorescence (*p*-RTP) nature. The prompt peaks at 375, 378 and 460 nm exhibit nanosecond lifetimes, confirming their assignment as fluorescence (Fig. S10†). In contrast, the prompt emission spectra of 10-Br-a are characterized by principal fluorescence peaks, with inconspicuous phosphorescence bands (Fig. S9†). The larger phosphorescence ratio (77%) of 10-Br-b, compared to 25% for 10-Br-a, leads to different PL colours under 254 nm irradiation. In addition, 10-Br-b demonstrates significantly enhanced *p*-RTP performance compared to 10-Br-a, displaying substantially longer phosphorescence lifetime (τ_p) and higher phosphorescence efficiency (Φ_p) of 882 ms and 8.8% by 2.2 and 8.0 times (Fig. 3e and f), respectively. This improvement is attributed to higher ISC and radiative triplet decay rates (k_{isc} and k_r^p), alongside lower nonradiative triplet decay rates of (k_{nr}^p) (Table 1), The more rigid conformation and denser packing in 10-Br-b, resulting from its bent molecular structure and the absence of water, effectively suppress nonradiative decay, thus enhancing triplet exciton generation and stability.

Analogous to 10-Br, 8-Br-b, with a more rigid conformation compared to 8-Br-a, displays improved *p*-RTP performance (Fig. S12 and S13†). However, unlike 10-Br, this discrepancy does not result in noticeable PL colour changes (Fig. 3a and S8†), likely due to the smaller increase in k_{isc} (1.1-fold) from 8-Br-a to 8-Br-b, compared to that of 10-Br (2.6-fold, Table 1). The relatively small difference in k_{isc} is primarily attributed to their similar linear conformations, which may lead to the formation of analogous ionic emissive clusters.

Meanwhile, three 10-I polymorphs exhibit green or yellowish-green PL (Fig. 3a and S8†). Due to extended electron delocalization facilitated by I^-,[36] the phosphorescence bands of 10-I are bathochromically shifted by 20 nm compared to 10-Br (Fig. 3d and S15b–S17b†). Furthermore, the stronger heavy atom effect of I^- enhances spin–orbit coupling (SOC) of 10-I, leading to increased k_{isc}, k_r^p and k_{nr}^p compared to 10-Br-a (Table 1). Notably, 10-I-MeCN features the most regular and compact molecular arrangement (Table S3†), with the highest packing density (1.434 g cm^{-3}), which is validated by its sharpest XRD peaks (Fig. S19†). As packing density increases, crystal efficiency (Φ_c) and τ_p progressively rise from 0.8% and 60 ms (10-I-H_2O) to 1.7% and 124 ms (10-I-MeOH), and finally to 4.2% and 216 ms (10-I-MeCN) (Fig. S15–S17 and Table S4†), demonstrating the role of conformational rigidity in PL regulation. In addition, the PL properties of these GAQAS polymorphs remain highly stable even after six months of storage(Fig. S20 and S21†).

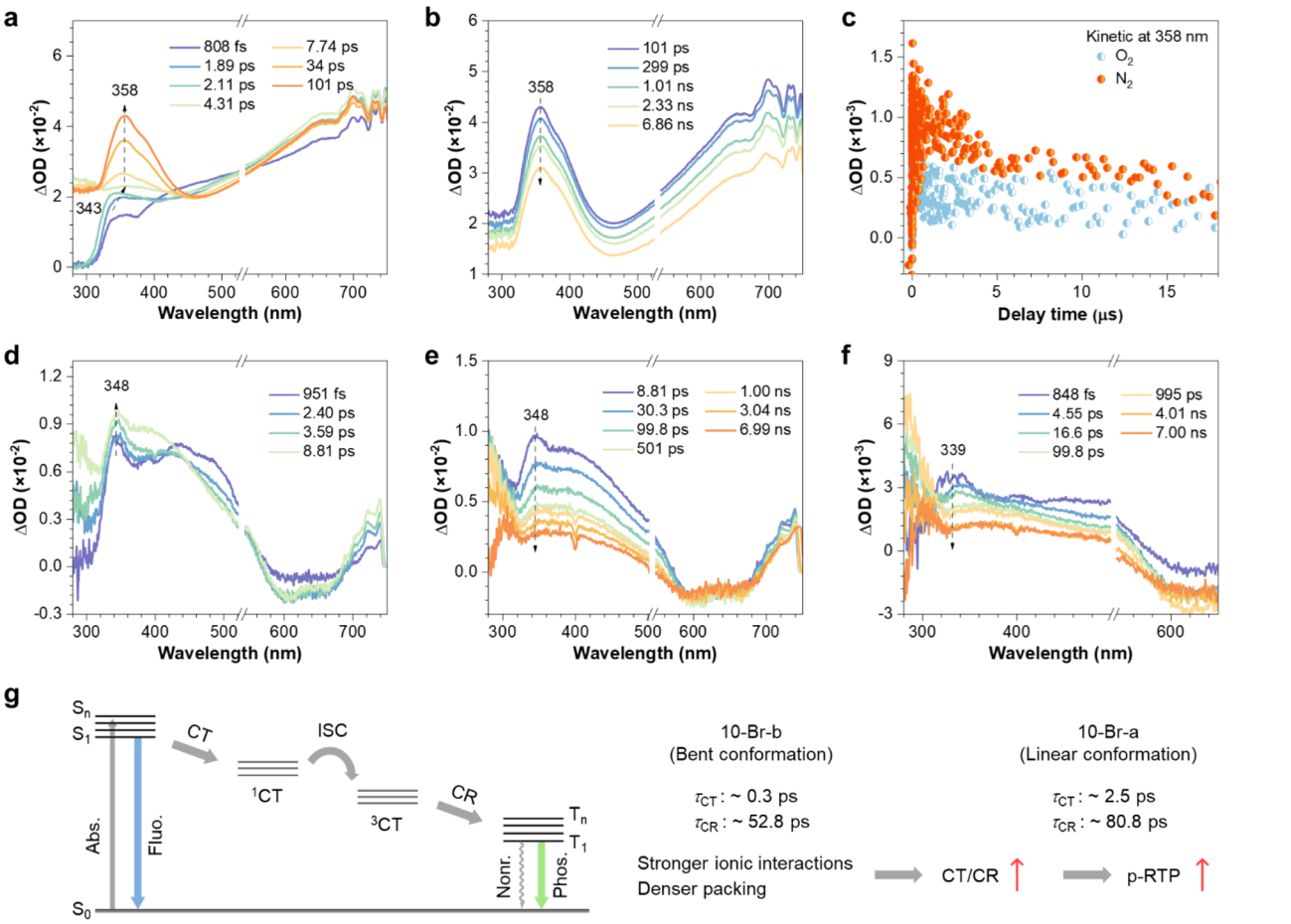

Fig. 4 (a and b) fs-TA spectra of 10-Br aqueous solution (2 M) after 266 nm UV excitation. (c) ns-TA spectra decay curve of 10-Br aqueous solution under N_2 and O_2 atmosphere. fs-TA spectra of (d and e) 10-Br-a and (f) 10-Br-b polymorphic powders after 266 nm UV irradiation. (g) The excited-state photophysical processes of 10-Br and the underlying reason for enhanced phosphorescence performance.

The above results indicate that conformational rigidity is essential for the enhancement of phosphorescence performance. To check it, pressurization and cryogenic experiments were conducted. Under 254 nm UV irradiation, applying pressure to 10-Br-a slightly improves its phosphorescence ratio, τ_p and Φ_c from 34%, 409 ms and 3.1% to 41%, 433 ms and 4.2%, respectively (Fig. S22†), benefiting from the enhanced short contacts and consequently conformational rigidification upon compression. Similarly, upon cooling to 77 K (λ_{ex} = 254 nm), abovementioned parameters increase to 60%, 783 ms and 11.6% for 10-Br-a and 86%, 1154 ms and 21.1% for 10-Br-b (Fig. S23, S24 and Table S5†), respectively. Surprisingly, despite the immense restriction of molecular motions at 77 K, the phosphorescence of 10-Br-a remains inferior to that of 10-Br-b at 298 K, indicating that clustering mode plays a more crucial role than conformational rigidity in driving enhanced phosphorescence in GAQAS polymorphs.

In addition to k_{nr}^{p}, which is closely related to conformational rigidity, distinct variations in k_{isc} and k_{r}^{p} are also noted for polymorphs (Table 1), which are crucial to the polymorphism-regulated emission. To further explore it, we employed ultrafast femtosecond to nanosecond transient absorption (fs/ns-TA) spectroscopy. When a 2 M aqueous solution of 10-Br is excited by a 266 nm pump beam, it exhibits an initial excited-state absorption (ESA) peak at 343 nm, which rapidly reaches its maximum and shifts to 358 nm within 4.31 ps. Subsequently, the 358 nm peak attains its maximum at 101 ps (Fig. 4a). Given the ionic nature of the ground state of 10-Br, this redshifted and intensified ESA peak is attributable to a charge transfer (CT) process.[37,38] Afterwards, the 358 nm ESA peak gradually decays, yet remains observable even after 6.86 ns, suggesting the high stability of this CT state (Fig. 4b). Further ns-TA kinetics reveals a faster decay rate under oxygen compared to nitrogen, indicating its triplet nature (Fig. 4c). The fs-TA kinetics at 358 nm shows the generation of triplet CT state (^{3}CT) and its conversion to a localized triplet state (charge combination, CR), with lifetimes of 22 (τ_1) and 598 ps (τ_2), respectively (Fig. S25a†).

The fs-TA kinetics of two 10-Br polymorphic powders also confirm the CT process. Due to the enhanced through-space electronic interactions in solids, the excited-state dynamics

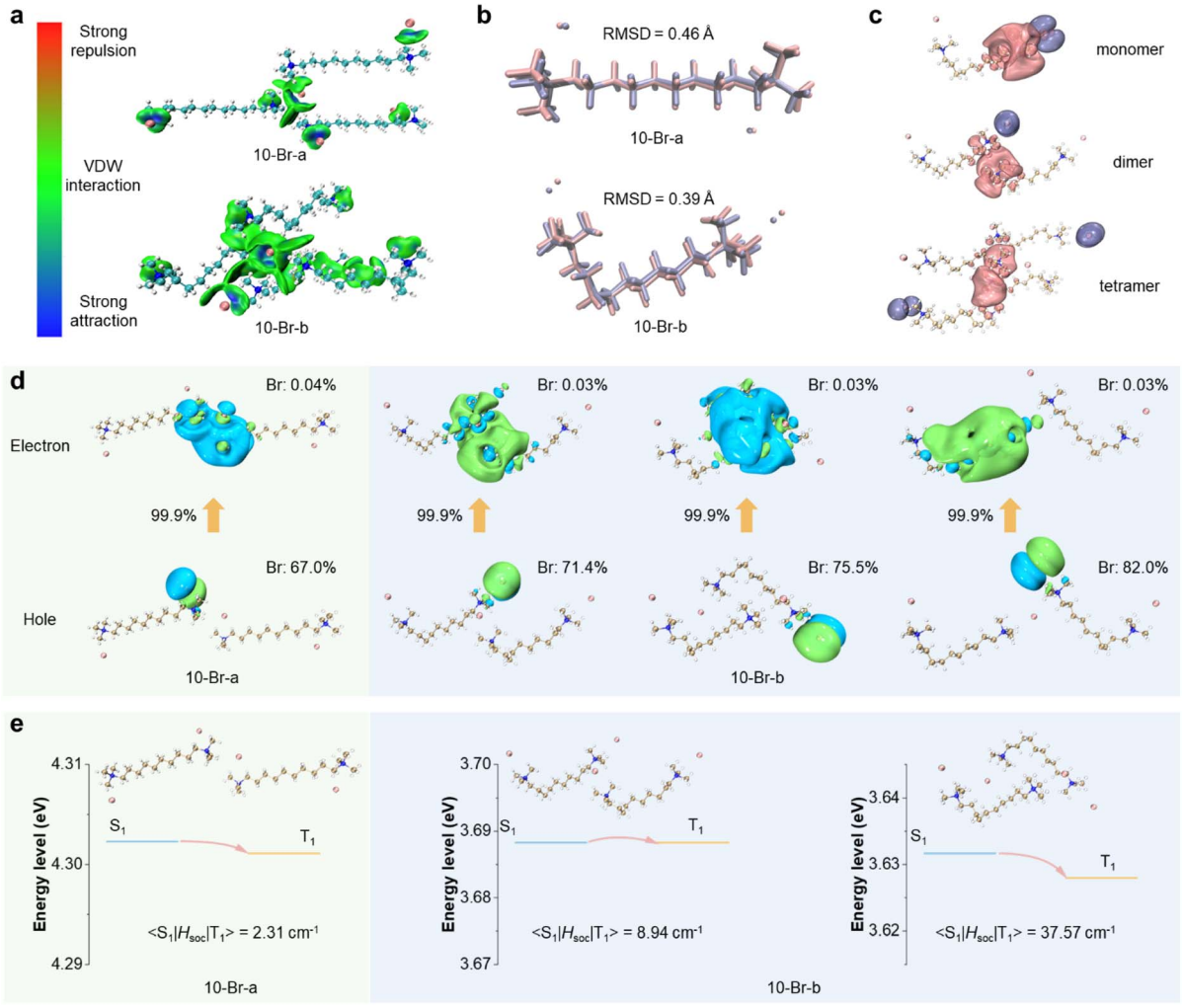

Fig. 5 (a) Noncovalent interactons (NCI) plots and (b) RMSD of 10-Br. (c) Hole–electron analysis of excited state of 10-Br-b (pink: electron, blue: hole). (d) The NTOs and corresponding proportions for 10-Br polymorphs, with the bromine components. (e) The calculated energy level diagram and SOC between singlets and triplets of 10-Br polymorphs.

are accelerated, preventing the observation of the initially rapid rise and red-shift of the CT ESA peak (Fig. 4d and f). For 10-Br-a, lifetimes for the CT and CR processes are 2.5 (τ_1) and 80.8 ps (τ_2), respectively (Fig. S25b†). In contrast, the generation of ^{3}CT in 10-Br-b is too rapid to be measured, allowing the observation only of the CR process, which exhibits a shorter lifetime of 52.8 ps (Fig. S25c†). The accelerated excited-state dynamics of 10-Br-b, arising from closer proximity of ionic pairs and stronger through-space electronic interactions, demonstrate its superior CT and CR, leading to enhanced k_r^p and *p*-RTP performance compared to 10-Br-a (Fig. 4g). Notably, the distinct CT ESA peaks for 10-Br-a and 10-Br-b, consistent with previous data, are indicative of the presence of different ionic clusters. This evidence strongly argues against impurity-induced emission, which would otherwise produce identical ESA peaks, and supports the CTE mechanism.

To further elucidate the underlying mechanism of polymorphism-regulated emission, theoretical calculations were performed. As depicted in Fig. 5a and b, much stronger intermolecular interactions in 10-Br-b, as well as lower root mean square deviation (RMSD) value (0.39 Å *vs.* 0.46 Å for 10-Br-a) which indicates weaker molecular flexibility, suggest more rigid conformations.[39] It is also noted that HOMOs are predominantly localized on Br^- anions, whereas LUMOs are mainly distributed on N^+ cations, denoting conspicuous CT and through-space conjugation characteristics (Fig. S27 and S28†). Moreover, from monomers to tetramers, enriched energy levels and narrowed energy gaps are found, which can rationalize the efficient PL of the crystals (Fig. S29†).

The natural transition orbitals (NTOs) analysis further reveals the clearly separated hole and electron distributions of 10-Br-b and underscores its through-space CT properties (Fig. 5c). Furthermore, the hole–electron overlap function index (S_r) and exciton binding energy (E_c), respectively describing the overlap degree and distribution range of hole–electron pairs,[40] show a decremental trend for 10-Br-b from 0.12 and 2.9 eV (monomer) to 0.001 and 1.9 eV (tetramer, Fig. S30†). This result indicates more separated hole–electron distribution and stronger CT of 10-Br upon aggregation. Notably, the NTOs of various 10-Br dimers show much higher Br^- component in the hole of 10-Br-b (≥71.4%) than 10-Br-a (67.0%, Fig. 5d), further demonstrating the enhanced CT in 10-Br-b. As for CR state, the NTOs and corresponding S_r and E_c values of the 10-Br-b dimer demonstrate obvious localized excitation (LE) characteriscs

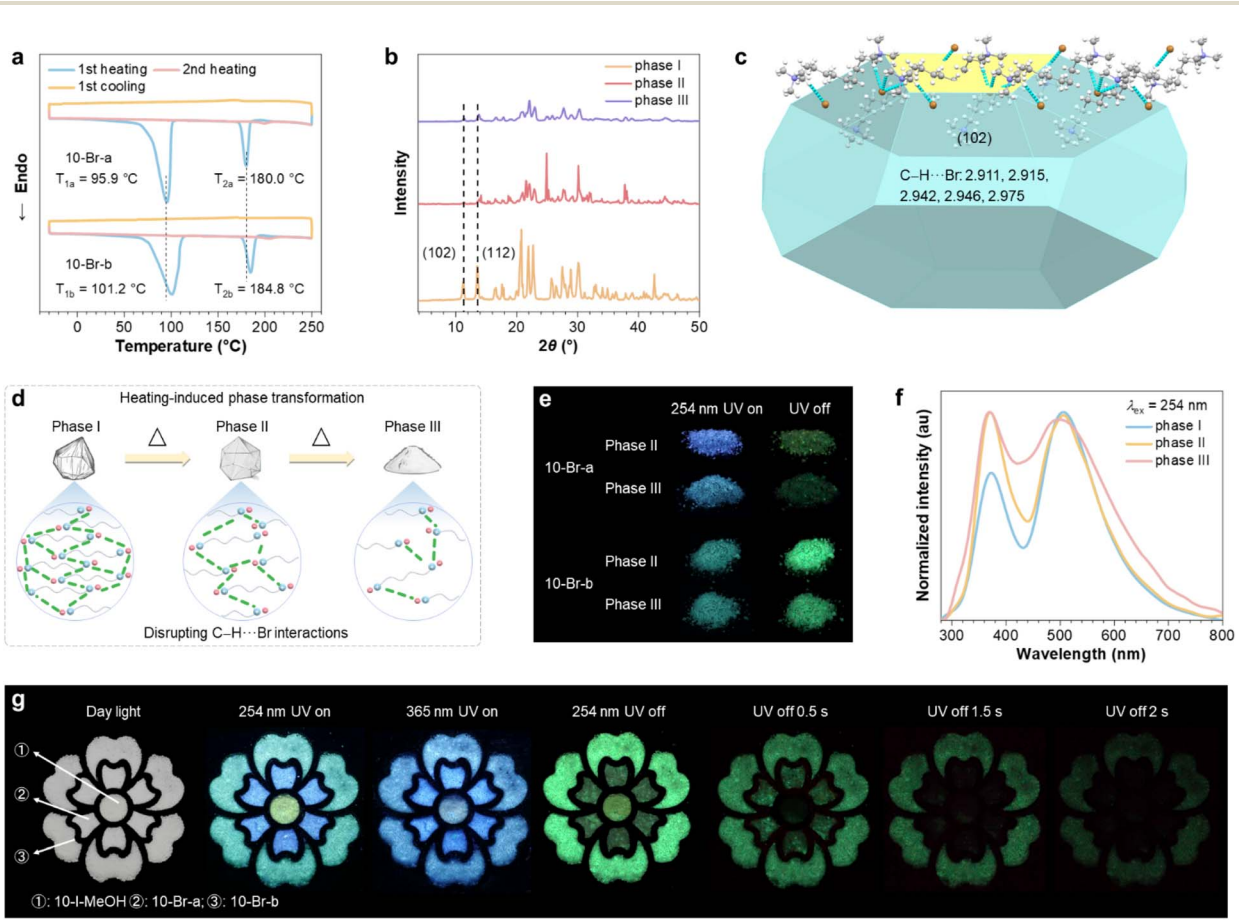

Fig. 6 (a) DSC curves of 10-Br-a and 10-Br-b (ramp rates = 5 °C·min^{-1}). (b) XRD spectra of different polymorphic phases of 10-Br-b. (c) Predicted crystal morphology and intermolecular interactions of 10-Br-b corresponding to the (102) plane. (d) Schematic illustration of heating-induced phase transformations of GAQASs. (e) Luminescent photographs of different 10-Br polymorphic phases under and after ceasing the 254 nm UV irradiation. (f) Prompt emission spectra of different 10-Br-b polymorphic phases. (g) Demonstration of the application in anti-counterfeiting.

(Fig. S31†). Meanwhile, 10-Br-b dimers exhibit larger SOC (Fig. 5e), likely originating from its enhanced heavy atom effect due to shorter ionic distances and stronger intermolecular interactions.[41,42] In a word, the polymorphism-regulated emission of GAQASs is primarily determined by distinct clustering states, arising from variations in molecular conformation and solvent interactions. Enhanced ionic clustering promotes CT/CR, the heavy atom effect and conformational rigidity, increasing k_r^P and k_{isc} while decreasing k_{nr}^P, ultimately affording boosted phosphorescence and readily tunable PL.

Notably, in addition to the distinct PL, these polymorphs also demonstrate two irreversible and different phase transformations,[43,44] as indicated by the DSC thermograms (Fig. 6a and S33†). During the first heating cycle, while 10-Br-b and 8-Br-b, possessing more rigid conformations, feature higher transformation temperatures of 101.2/184.8 and 99.0/208.4 °C, the corresponding transformation temperatures for their polymorphic counterparts are 95.9/180.0 and 84.4/205.0 °C, respectively. These transformations are likely due to the disruption of intermolecular interactions. Upon transitioning from phase I to phase II and then to phase III, the sharp diffraction peaks progressively broaden and weaken, demonstrating the destruction of crystalline structure (Fig. 6b and S34†). Further growth morphology modeling, using the Bravais-Friedel Donnay-Harker method,[45] again supports this hypothesis. The signal for the phase I of 10-Br-b at $2\theta = 13.5°$, corresponding to the (102) plane, dramatically diminishes, implying an adjusted molecular arrangement through disruption of relevant C–H···Br interactions (Fig. 6c). Similarly, the depressed peak at $2\theta = 13.7°$ indicates the altered molecular arrangement along the (110) plane in 10-Br-a (Fig. S34 and S35†). Therefore, the progressive destruction of crystalline structures and intermolecular interactions occurrs during phase transformations (Fig. 6d), which would deteriorate the PL properties. For instance, the PL colour of phase II of 10-Br-a is dark blue, shifting to blue-cyan for phase III, accompanied by a red-shifted prompt PL peak from 400 to 435 nm (Fig. 6e, S36 and S37†). In contrast, 10-Br-b exhibits minimal variation in both PL and afterglow colours across its different phases, displaying changes primarily in the relative intensity of its dual emissions (Fig. 6f and S39†). Meanwhile, from phase I to phase III, τ_p and Φ_c of 10-Br-a/b gradually decrease from 409/882 ms and 3.1/11.5% to 159/639 and 2.3/6.3%, and finally to 140/234 ms and 1.1/2.4% (Fig. S38, S40 and Table S4†), accompanying increased non-radiative decay rates (Table S9†). Impressively, phase transformations of 10-Br polymorphs lead to variations in emissive clusters and consequently different excitation spectra (Fig. S41†), thus further supporting the CTE mechanism.

The PL regulation achieved through polymorphism and phase transformation endows GAQASs with strong potential for applications such as data encryption and anticounterfeiting applications. For instance, the 'flower' pattern is created using 10-Br-a, 10-Br-b and 10-I-MeOH (Fig. 6g). Under 254 nm UV irradiation, a polychrome 'flower' is visualized, which shifts to blue under 365 nm UV excitation. After ceasing the 254 nm UV irradiation, an immediate green 'flower' is observed, which evolves into different patterns over time due to their comparable, yet distinct, phosphorescence lifetimes of the polymorphs.

Conclusions

In summary, to tune the PL and moreover to elucidate the luminescent mechanism of NCLs, we investigated the polymorphism and phase transformation behaviour of 10-Br, 8-Br and 10-I GAQASs, revealing their tunable emissions. Specifically, molecular conformation and solvent interactions significantly influenced molecular packing, which in turn affected electron delocalization and conformational rigidity. Denser ionic clustering and more rigidified conformations led to enhanced phosphorescence, enabling readily tunable PL in various polymorphs and phases. Moreover, ultrafast spectroscopy and theoretical results revealed that enhanced ionic clustering endows polymorphs with more effective CT/CR, improved heavy atom effect and more rigid conformations, leading to the increased k_r^P/k_{isc} and decreased k_{nr}^P, thereby boosting phosphorescence. These findings not only provide insights into the detailed exciton dynamics and definitively exclude oxidation and impurity as the origin of luminescence in these highly purified NCLs, but also offer a viable strategy for regulating their PL properties through polymorphism and phase transformation.

Data availability

The data supporting this article are present in the manuscript and/or ESI.† Crystallographic data for 10-Br-a, 10-Br-b, 8-Br-a, 8-Br-b, 10-I-H_2O, 10-I-MeOH and 10-I-MeCN has been deposited at the CCDC.

Author contributions

W. Z. Y. conceived the initial project. A. L. and W. Z. Y. designed the experiments. A. L. conducted the synthesis, spectroscopic characterization, and single-crystal analysis. G. Y. performed the ultrafast spectroscopy and assisted A. L. in data analyses. A. L. performed the purification and purity characterization of chemicals. A. L., Z. Z. and Q. Z. carried out the theoretical calculations and analysed the results. Z. Z. and X. C. support A. L. in draft manuscript. W. Z. Y. supervised the project and revised the manuscript. All authors have given approval to the final version of the manuscript.

Conflicts of interest

There are no conflicts to declare.

Acknowledgements

This work was financially supported by the National Natural Science Foundation of China (U22A20250 and 52473185).

References

1 B. Chu, X. Liu, X. Li, Z. Zhang, J. Z. Sun, Q. Yang, B. Liu, H. Zhang, C. Zhang and X.-H. Zhang, *J. Am. Chem. Soc.*, 2024, **146**, 10889.
2 Y. He, Y. Qiao, Z. Li, W. Feng, Y. Zhao, W. Tian, B. Z. Tang and H. Yan, *Angew. Chem., Int. Ed.*, 2024, **63**, e202413425.
3 C.-Y. Shi, D.-D. He, B.-S. Wang, Q. Zhang, H. Tian and D.-H. Qu, *Angew. Chem., Int. Ed.*, 2023, **62**, e202214422.
4 X. Ji, W. Tian, K. Jin, H. Diao, X. Huang, G. Song and J. Zhang, *Nat. Commun.*, 2022, **13**, 3717.
5 J. Pansieri, V. Josserand, S.-J. Lee, A. Rongier, D. Imbert, M. M. Sallanon, E. Kövari, T. G. Dane, C. Vendrely, O. Chaix-Pluchery, M. Guidetti, J. Vollaire, A. Fertin, Y. Usson, P. Rannou, J.-L. Coll, C. Marquette and V. Forge, *Nat. Photonics*, 2019, **13**, 473.
6 D. A. Tomalia, B. Klajnert-Maculewicz, K. A.-M. Johnson, H. F. Brinkman, A. Janaszewska and D. M. Hedstrand, *Prog. Polym. Sci.*, 2019, **90**, 35.
7 H. Li, J. Gu, Z. Wang, J. Wang, F. He, P. Li, Y. Tao, H. Li, G. Xie, W. Huang, C. Zheng and R. Chen, *Nat. Commun.*, 2022, **13**, 429.
8 Q. Fan, Y. Tang, H. Sun, D. Guo, J. Ma and J. Guo, *Adv. Mater.*, 2024, **36**, 2401315.
9 N. Jiang, C.-Y. Zhu, K.-X. Li, Y.-H. Xu and M. R. Bryce, *Macromolecules*, 2024, **57**, 5561.
10 W. I. Lee, Y. Bae and A. J. Bard, *J. Am. Chem. Soc.*, 2004, **126**, 8358.
11 A. Pucci, R. Rausa and F. Ciardelli, *Macromol. Chem. Phys.*, 2008, **209**, 900.
12 Z. Wu, J. C. Roldao, F. Rauch, A. Friedrich, M. Ferger, F. Würthner, J. Gierschner and T. B. Marder, *Angew. Chem., Int. Ed.*, 2022, **61**, e202200599.
13 A. Mazarevics, K. Leduskrasts and E. Suna, *ACS Mater. Lett.*, 2024, **6**, 2703.
14 F. T. S. Chan, G. S. Kaminski Schierle, J. R. Kumita, C. W. Bertoncini, C. M. Dobson and C. F. Kaminski, *Analyst*, 2013, **138**, 2156.
15 A. D. Stephens, M. N. Qaisrani, M. T. Ruggiero, G. Díaz Mirón, U. N. Morzan, M. C. González Lebrero, S. T. E. Jones, E. Poli, A. D. Bond, P. J. Woodhams, E. M. Kleist, L. Grisanti, R. Gebauer, J. A. Zeitler, D. Credgington, A. Hassanali and G. S. Kaminski Schierle, *Proc. Natl. Acad. Sci. U.S.A.*, 2021, **118**, e2020389118.
16 J. Deng, H. Liu, D. Liu, L. Yu, Y. Bai, W. Xie, T. Li, C. Wang, Y. Lian and H. Wang, *Adv. Funct. Mater.*, 2024, **34**, 2308420.
17 S. Tang, T. Yang, Z. Zhao, T. Zhu, Q. Zhang, W. Hou and W. Z. Yuan, *Chem. Soc. Rev.*, 2021, **50**, 12616.
18 Z. Zhao, A. Li and W. Z. Yuan, *Acc. Chem. Res.*, 2025, **58**, 612.
19 F. Nie and D. Yan, *Nat. Commun.*, 2024, **15**, 9491.
20 C. Li, O. Arteaga, F. Ehlers, M. Krüsmann, B. Sun, J. Poisson, M. Karg, P. Vana and K. Zhang, *Aggregate*, 2024, e695.
21 M. Mahapatra, M. Bourguignon, B. Grignard, M. Vandevenne, M. Galleni and C. Detrembleur, *Angew. Chem., Int. Ed.*, 2025, **64**, e202413605.
22 X. Chen, C. Hu, Y. Wang, T. Li, J. Jiang, J. Huang, S. Wang, W. Dong and J. Qiao, *Adv. Sci.*, 2024, **11**, 2304946.
23 X. Li, Y. Yang, Z. Zhao, S. Bai, Q. Li and J. Li, *Angew. Chem., Int. Ed.*, 2024, e202422272.
24 Y. He, W. Feng, Y. Qiao, Z. Tian, B. Z. Tang and H. Yan, *Angew. Chem., Int. Ed.*, 2023, **62**, e202312571.
25 L. Vallan, A. T. Bui, G. Jonusauskas, N. D. McClenaghan, E. Istif, D. Mantione, E. Pavlopoulou, C. Brochon, G. Hadziioannou and E. Cloutet, *Macromolecules*, 2023, **56**, 4541.
26 K. M. Steed and J. W. Steed, *Chem. Rev.*, 2015, **115**, 2895.
27 A. J. Cruz-Cabeza, S. M. Reutzel-Edens and J. Bernstein, *Chem. Soc. Rev.*, 2015, **44**, 8619.
28 Y. Chen, A. Li, X. Li, L. Tu, Y. Xie, S. Xu and Z. Li, *Adv. Mater.*, 2023, **35**, 2211917.
29 B. Lu, S. Liu and D. Yan, *Chin. Chem. Lett.*, 2019, **30**, 1908.
30 C. Zhao, Y. Wang, Y. Jiang, N. Wu, H. Wang, T. Li, G. Ouyang and M. Liu, *Adv. Mater.*, 2024, **36**, 2403329.
31 Y. Lai, Z. Zhao, S. Zheng and W. Z. Yuan, *Acta Chim. Sin.*, 2021, **79**, 93.
32 S. Tang, Z. Zhao, J. Chen, T. Yang, Y. Wang, X. Chen, M. Lv and W. Z. Yuan, *Angew. Chem., Int. Ed.*, 2022, **61**, e202117368.
33 A. Li, S. Tang, Z. Zhao, Q. Zhang, Y. Cai and W. Z. Yuan, *Adv. Opt. Mater.*, 2024, **12**, 2400262.
34 R. Dubey and G. R. Desiraju, *Angew. Chem., Int. Ed.*, 2014, **53**, 13178.
35 K. Suresh, T. Mehta, V. Thakrar and R. G. Sharma, *Cryst. Growth Des.*, 2025, **25**, 1282.
36 T. Zhu, T. Yang, Q. Zhang and W. Z. Yuan, *Nat. Commun.*, 2022, **13**, 2658.
37 G. Yang, S. Hao, X. Deng, X. Song, B. Sun, W. J. Hyun, M.-D. Li and L. Dang, *Nat. Commun.*, 2024, **15**, 4674.
38 T.-C. Lin, M. Sarma, Y.-T. Chen, S.-H. Liu, K.-T. Lin, P.-Y. Chiang, W.-T. Chuang, Y.-C. Liu, H.-F. Hsu, W.-Y. Hung, W.-C. Tang, K.-T. Wong and P.-T. Chou, *Nat. Commun.*, 2018, **9**, 3111.
39 L. Wang, Z. Xiong, J. Z. Sun, F. Huang, H. Zhang and B. Z. Tang, *Angew. Chem., Int. Ed.*, 2024, **63**, e202318245.
40 Z. Liu, T. Lu and Q. Chen, *Carbon*, 2020, **165**, 461.
41 Q. Zheng, Y.-K. Qu, P. Zuo, H.-T. Yuan, Y.-J. Yang, Y.-C. Qiu, L.-S. Liao, D.-Y. Zhou and Z.-Q. Jiang, *Chem*, 2025, **11**, 102353.
42 S. Jiang, D. Liu, Z. Chen, Z. Yang, Y. He, G.-X. Yang, D. Li and S.-J. Su, *Adv. Funct. Mater.*, 2024, **34**, 2316355.
43 J. Wang, T. Zhang, Z.-X. Zhang, C.-Y. Su, Y. Zhang and D.-W. Fu, *Inorg. Chem.*, 2020, **59**, 16635.
44 Y.-L. Wei, J. Jing, C. Shi, H.-Y. Ye, Z.-X. Wang and Y. Zhang, *Chem. Commun.*, 2018, **54**, 8076.
45 X. Ye, Y. Liu, Q. Guo, Q. Han, C. Ge, S. Cui, L. Zhang and X. Tao, *Nat. Commun.*, 2019, **10**, 761.